Letters

Experimental Parameter Extraction of the Full-Order Impedance Matrix Model for the High-Frequency Magnetic Link of an MAB Converter

Ayooluwa Ajiboye, *Member, IEEE*, Chanaka Singhabahu, *Member, IEEE*, Benjamin Shani, *Graduate Student Member, IEEE*, Hassan Habib Chaudhry, *Graduate Student Member, IEEE*, and Alireza Khaligh, *Senior Member, IEEE*

***Abstract*—This work proposes a single-port measurement scheme for extracting the impedance matrix (Z-matrix) model parameters for the high-frequency magnetic link (HFML) of a multiactive bridge (MAB) converter, as opposed to individual, error-prone, two-port concurrent voltage–current measurements. The Z-matrix is extracted over a wide-frequency range to estimate the HFML branch currents relative to other existing HFML models. The accuracy of the extracted Z-matrix is verified by comparing the analytical estimates to steady-state experiments conducted on a 3.2 kW SiC four-port MAB prototype. The improved accuracy of the Z-matrix over existing HFML models validates the proposed single-port parameter extraction method.**

***Index Terms*—Delta (Δ), extended cantilever model (ECM), frequency domain, GHA, multiactive bridge (MAB), multiport, quad active bridge (QAB), star (Y), triple active bridge (TAB).**

I. Introduction

MULTIACTIVE bridge (MAB) converters are widely renowned for their versatile reconfigurable nature as they facilitate power transfer between multifarious energy sources and loads [1], [2]. In recent years, MAB converters have become a preferred multiport solution in applications, such as energy routers, microgrids, and transportation electrification [3]. The structure of the n-port MAB is comprised of multiple full- or half- bridge switching cells interconnected through a mutually shared high-frequency magnetic link (HFML). The galvanically isolated multiterminal HFML consists of a centralized transformer structure with a network of series branch inductors either integrated or externally connected. The topology of the four-port MAB [that is, quad-active-bridge (QAB)] converter including its HFML is demonstrated in Fig. 1.

A precise model of the HFML enables the accurate estimation of its branch currents, which in turn facilitates an accurate theoretical prediction of the converter's multidirectional power flow. Beyond modeling the ac magnetic link, an accurate and systematic parameter extraction scheme for the HFML model is required to reliably characterize the n-port MAB converter operation. In this regard, several techniques have been used to model the multiwinding HFML in existing MAB-related literature. The works in [4] and [5] utilize the Y-Δ model for port-wise power flow estimation, where the Δ-model parameters are calculated from the extracted Y-model using a Thevenin approach [6]. The reduced-order nature of the Y-Δ approach precludes it from capturing the full nonuniform cross-coupling behavior of the HFML especially for integrated-leakage structures with complex geometries [7], [8]. In addition, the experimental parameter extraction of the Y-model yields inconsistent solutions due to unavoidable measurement errors coupled with its reduced-order nature, which in turn impacts the accuracy of the calculated Δ-model. In [9], the extended cantilever model (ECM) is used to model the multiwinding HFML structure. The ECM parameter extraction requires concurrent two-port voltage–current measurements. As such, measurement errors due to nonnegligible short-circuit and current-sensor impedances [10] impact its accuracy despite being a full-order model [7], [11]. The requirement of multiple simultaneous low-impedance short circuits along with concurrent two-port probe-measurements increases

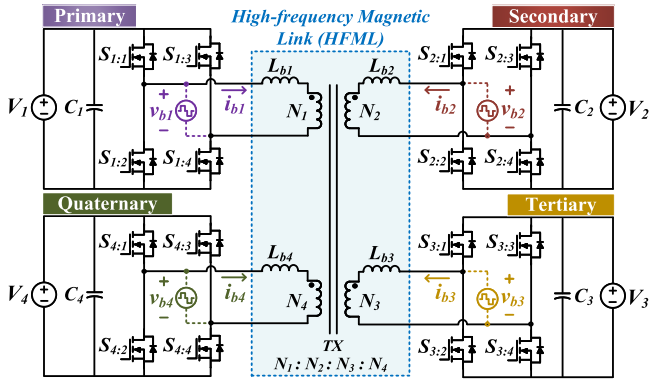

Fig. 1. Four-port MAB—Quad-active-bridge (QAB) converter with an high-frequency magnetic link (HFML).

Received 10 July 2025; revised 28 August 2025; accepted 6 October 2025. Date of publication 9 October 2025; date of current version 13 November 2025. *(Corresponding author: Ayooluwa Ajiboye.)*

The authors are with the Maryland Power Electronics Laboratory, Department of Electrical and Computer Engineering, Institute for Systems Research, University of Maryland, College Park, MD 20742 USA (e-mail: ajiboye1@umd.edu; chanaka@terpmail.umd.edu; shani@umd.edu; hassanh@umd.edu; khaligh@umd.edu).

Color versions of one or more figures in this article are available at https://doi.org/10.1109/TPEL.2025.3619538.

Digital Object Identifier 10.1109/TPEL.2025.3619538

TABLE I
COMPARISON OF PARAMETER EXTRACTION METHODS FOR THE HFML MODELS OF THE QAB CONVERTER

Reference	Model	Order type	Extraction method	Extracted parameters	Extraction difficulty	Error susceptibility	Parasitics included?	Computational burden	Extraction accuracy
[4], [5]	Y-Δ	Reduced-order	Experimental (single-port)	5	Low	High	No	Low	Low
[9], [11]	ECM	Full-order	Experimental (two-port)	10	High	High	No	Medium	Medium
[2], [12]	Inductance matrix	Full-order	FEA simulation	10	High	Medium	Yes	High	High
This work	Impedance matrix	Full-order	Experimental (single-port)	10	Low	Low	Yes	Low	High

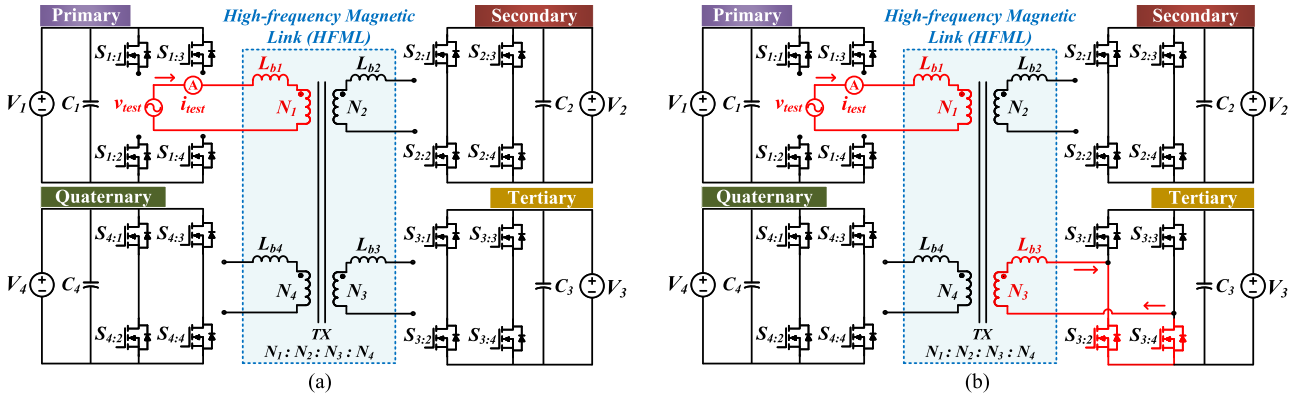

Fig. 2. Single-port measurement procedure for MAB HFML **Z**-matrix parameter extraction using an impedance analyzer. (a) Self-impedance open-circuit measurement using $z_{11,k}$ example. (b) Input impedance measurement under hybrid open-circuit and short-circuit conditions using $z_{meas,13,k}$ example.

the error susceptibility of the ECM model. The works in [2] and [12], introduce the $n \times n$ full-order self-/mutual- inductance matrix developed into an impedance matrix as the MAB HFML model. A notable drawback of this approach is its reliance on a finite-element-analysis (FEA) simulation framework for the formulation of the impedance matrix, as opposed to an experimentally derived impedance matrix capable of capturing the practical nonidealities of the HFML stack-up.

To overcome these limitations, this letter presents an experimental approach based on single-port impedance measurements for the formulation of a full-order $n \times n$ impedance matrix (**Z**-matrix) of the HFML. The accurate extraction of the **Z**-matrix model parameters enables the precise estimation of the branch currents, leading to a comprehensive and reliable model of the MAB converter operation. In Table I, a detailed comparison of the parameter extraction methods of the considered HFML models with respect to the proposed approach is provided. In addition, steady-state experimental results are presented to verify the accuracy improvement of the extracted **Z**-matrix relative to existing MAB HFML extracted models.

II. EXTRACTING THE IMPEDANCE MATRIX PARAMETERS USING A SINGLE-PORT MEASUREMENT SCHEME

In this section, a novel single-port impedance measurement scheme is introduced to experimentally extract the **Z**-matrix parameters using a frequency-domain port-network analytical framework. Consider the frequency-domain kth-harmonic four-port impedance network expressed in

$$\begin{bmatrix} v_{b1,k} \\ v_{b2,k} \\ v_{b3,k} \\ v_{b4,k} \end{bmatrix} = \begin{bmatrix} z_{11,k} & z_{12,k} & z_{13,k} & z_{14,k} \\ z_{21,k} & z_{22,k} & z_{23,k} & z_{24,k} \\ z_{31,k} & z_{32,k} & z_{33,k} & z_{34,k} \\ z_{41,k} & z_{42,k} & z_{43,k} & z_{44,k} \end{bmatrix} \begin{bmatrix} i_{b1,k} \\ i_{b2,k} \\ i_{b3,k} \\ i_{b4,k} \end{bmatrix} \tag{1}$$

where $v_{bx,k}$ and $i_{bx,k}$ represent the xth port transformer branch voltage and current for the kth-harmonic. Also, $z_{xx,k}$ and $z_{xy,k}$ denote the kth-harmonic self- and mutual- impedance elements. Ports 1, 2, 3, and 4 are alternatively referred to as the primary, secondary, tertiary, and quaternary ports.

Owing to the $n(n+1)/2$ criterion and magnetic reciprocity [9], 10 independent parameter measurements are required for the construction of the four-port **Z**-matrix. In this regard, Fig. 2 demonstrates the single-port impedance-measurement procedure for experimentally constructing the HFML **Z**-matrix. Note that the combination of v_{test} and i_{test} represents an impedance analyzer measurement. As shown in Fig. 2(a), $z_{xx,k}$ is determined via open-circuit measurements which results in (2), and thereby prevents any measurement skews due to the nonlinear output capacitances of the switching devices [13], [14]

$$z_{xx,k} = \left. \frac{v_{bx,k}}{i_{bx,k}} \right|_{i_{bj,k}=0, \text{ where } j \neq x}. \tag{2}$$

Furthermore, to determine the $z_{xy,k}$ elements, input impedance measurements (denoted by $z_{\text{meas},xy,k}$) with the hybrid combination of open- and short- circuit conditions are required, as illustrated in Fig. 2(b), using the $z_{\text{meas},13,k}$ example. Considering x and y ports from (1), measuring the xth-port input impedance while short-circuiting the yth port, and open-circuiting every other j port results in (3). Short-circuits are introduced by turning on the bottom-side switches (or top-side switches alternatively) as shown in Fig. 2(b) in order to capture the switches' ON-state parasitic elements.

$$\begin{aligned} v_{bx,k} &= z_{xx,k} \cdot i_{bx,k} + z_{xy,k} \cdot i_{by,k}\,|_{i_{bj,k=0}} \\ v_{by,k} = 0 &= z_{yx,k} \cdot i_{bx,k} + z_{yy,k} \cdot i_{by,k}\,|_{i_{bj,k=0}}. \end{aligned} \tag{3}$$

Rearranging (3) while considering $z_{xy,k} = z_{yx,k}$ symmetry results in the $z_{\text{meas},xy,k}$ expression given in (4)

$$z_{\text{meas},xy,k} = \left.\frac{v_{bx,k}}{i_{bx,k}}\right|_{\substack{v_{by,k=0} \\ i_{bj,k=0}}} = \frac{z_{xx,k} \cdot z_{yy,k} - z_{xy,k}^2}{z_{yy,k}}. \tag{4}$$

Therefore, the generic form of the xth port mutual-impedance $z_{xy,k}$ derived from (4) is provided in (5)

$$z_{xy,k} = \sqrt{z_{xx,k} \cdot z_{yy,k} - z_{\text{meas},xy,k} \cdot z_{yy,k}}. \tag{5}$$

It is worth noting that the impedance analyzer placement in the proposed single-port measurement scheme shown in Fig. 2 can be slightly modified, if necessary, to account for additional power loop parasitic elements in the dc-link power path. Moreover, the constructed **Z**-matrix from the above-mentioned generalized single-port measurement scheme can be subsequently utilized in generalized harmonic analysis (GHA) to evaluate the HFML branch currents. For an accurate GHA model, the **Z**-matrix model parameters can be extracted over a wide frequency range, thereby capturing the impedance response across multiple harmonics. This enables the inclusion of frequency-dependent HFML nonidealities, such as the ac resistances due to skin and proximity effects within the full-order impedance matrix.

III. GHA Using Impedance Matrix

The GHA approach entails the Fourier decomposition of the HFML branch voltages into individual harmonic components [5]. The Fourier time-domain reconstruction of the xth port branch voltage denoted by $v_{bx}(t)$ is expressed in (6). $\overrightarrow{V_{bx,k}}$ represents the kth-harmonic coefficient of the branch voltage and is expressed in (7). φ_x and δ_x represent the outer and inner phase-shifts with respect to the primary port. V_x represents the xth port dc-link voltage, $k_{\max}$ represents the maximum harmonic, ω_{sw} is the angular switching frequency ($2\pi f_{\text{sw}}$), and $x \in [1, n]$ where n denotes the number of ports

$$v_{bx}(t) = \sum_{k=1,\ \text{odd}}^{k_{\max}} \left|\overrightarrow{V_{bx,k}}\right| \sin\left(k\omega_{\text{sw}}t + \angle\overrightarrow{V_{bx,k}}\right) \tag{6}$$

$$\overrightarrow{V_{bx,k}} = \frac{4V_x}{k\pi}\ \cos\left(k\delta_{\text{x}}\right) e^{-jk\varphi_{\text{x}}}. \tag{7}$$

By rearranging (1), the kth-harmonic branch current phasors ($\overrightarrow{I_{bx,k}}$) can be calculated, as shown in (8). $\mathbf{I_k}$ and $\mathbf{V_k}$ are $n \times 1$ column matrices consisting of $\overrightarrow{I_{bx,k}}$ and $\overrightarrow{V_{bx,k}}$ respectively

$$\mathbf{I_k} = \mathbf{Z_k^{-1}}\ \mathbf{V_k}. \tag{8}$$

By leveraging the kth-harmonic current phasors ($\overrightarrow{I_{bx,k}}$) as presented in [12], the root-mean-square (rms) and peak values of the branch currents can be calculated from (9) and (10) respectively

$$i_{bx,\text{rms}} = \sqrt{\sum_{k=1,\ \text{odd}}^{k_{\max}} \frac{1}{2}\left(\overrightarrow{I_{bx,k}} \cdot \overrightarrow{I_{bx,k}}^{*}\right)} \tag{9}$$

$$i_{bx,\max} = \max\left(\sum_{k=1,\ \text{odd}}^{k_{\max}} \left|\overrightarrow{I_{bx,k}}\right| \sin\left(k\omega_{\text{sw}}t + \angle\overrightarrow{I_{bx,k}}\right)\right). \tag{10}$$

It should be noted that the above-mentioned GHA framework assumes a 50% switch duty-cycle. In cases where there are asymmetric duty cycles of the half-bridge pole voltages of a full-bridge port, a dc bias voltage is introduced, along with both even and odd harmonics. The even and odd harmonics can be readily captured through the Fourier decomposition of the pole voltages, which are subsequently subtracted to calculate the branch voltages. The expression in (8) can then be utilized to estimate the ac behavior of the branch currents. Whereas the dc bias currents are obtained by inverting the resistance matrix derived from the real part of the **Z**-matrix and multiplying it with the average pole voltages. Alternatively, the impedance of any introduced dc-blocking capacitors can also be effectively captured within the full-order $n \times n$ **Z**-matrix.

The analytical HFML branch currents from the above-mentioned GHA construct are later used in Section V to benchmark the extracted **Z**-matrix accuracy against existing HFML models.

IV. Asymmetric Integrated-Leakage HFML

In this work, the HFML comprises of a litz-wire-based asymmetric integrated-leakage multiwinding structure, as shown in Fig. 3. A hybrid center- and side-limb winding configuration similar to the method in [8] is utilized. Table II summarizes the parameters of the implemented asymmetric integrated-leakage HFML. The extraction sequence from Section II is applied to the implemented integrated-leakage HFML in order to formulate the **Z**-matrix and benchmark its accuracy against the ECM [9] and Y-Δ model [4].

V. Experimental Results and Discussion

A. Hardware Setup

A SiC-based QAB prototype is developed as shown in Fig. 4 to validate the proposed methodology. The electrical specifications of the QAB hardware prototype are summarized in Table III.

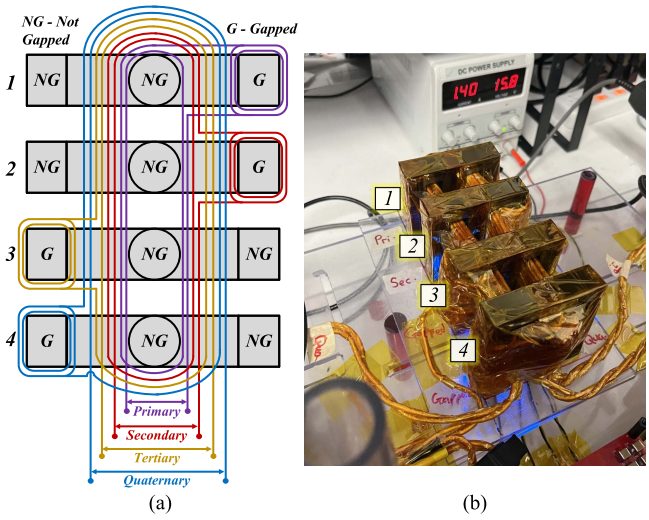

Fig. 3. Asymmetric integrated-leakage multiwinding magnetic structure. (a) Cross-sectional top-view layout. (b) Fully assembled HFML stackup.

TABLE II
PARAMETERS OF THE ASYMMETRIC INTEGRATED-LEAKAGE MAGNETIC STRUCTURE

Parameter	Primary (Port 1)	Secondary (Port 2)	Tertiary (Port 3)	Quaternary (Port 4)
Core type	EC70/34/17-3C94			
Core arrangement	1	2	3	4
Magnetizing branch	Center-limb			
Magnetizing airgap	0.2 mm			
Magnetizing turns	16	16	16	16
Turns ratio	1 : 1 : 1 : 1			
Leakage limb	Right	Right	Left	Left
Leakage airgap	2 mm	2.5 mm	2.5 mm	3 mm
Leakage turns	9	16	16	15

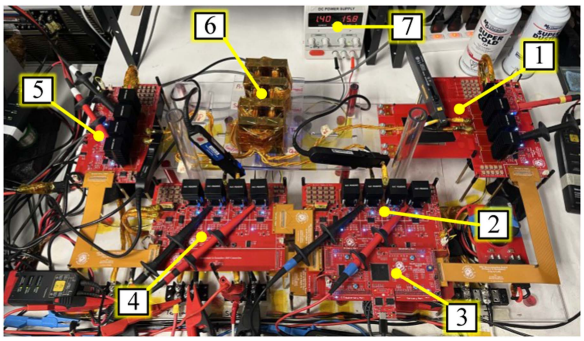

Fig. 4. QAB prototype setup. (1) Primary port. (2) Secondary port. (3) DSP microcontroller. (4) Tertiary port. (5) Quaternary port. (6) Asymmetric integrated-leakage HFML. (7) Auxiliary power supply.

The four ports are configured in one-source, three-load (1S-3L) mode with the primary serving as the source port.

B. HFML Model Parameter Extraction Results

The ten independent impedance parameters of the four-port **Z**-matrix are extracted using a Keysight E4990A impedance analyzer while following the proposed single-port impedance measurement scheme (see Section II). Several harmonics are extracted to account for HFML frequency-dependencies and overall improved model accuracy [5]. To illustrate some of the impedance measurement results, Fig. 5 presents the resulting frequency response of the z_{11} and z_{12} impedance elements across a 1 kHz–10 MHz frequency range. Similarly, the remaining **Z**-matrix parameters are extracted, and the fundamental harmonic component of the overall **Z**-matrix is expressed in (11) shown at the bottom of this page.

TABLE III
QAB PROTOTYPE ELECTRICAL SPECIFICATIONS

Parameter	Primary	Secondary	Tertiary	Quaternary
Configuration	Input	Output	Output	Output
Max. voltage rating	400 V	440 V	300 V	240 V
Max. power rating	3.2 kW	1.3 kW	0.9 kW	1.0 kW
DC-link capacitance	140 μF	26 μF	26 μF	26 μF
Switching frequency	100 kHz			
DSP microcontroller	TMS320F28388D			
SiC MOSFET	SCT4018KR (ROHM)			

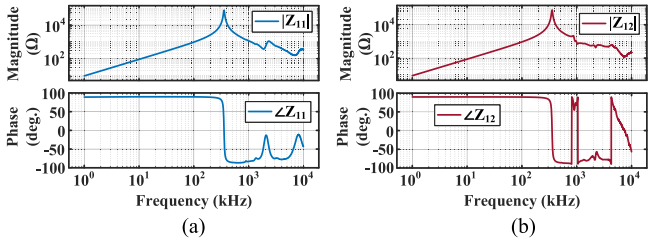

Fig. 5. Frequency response (bode plots) of z_{11} self- and z_{12} mutual-impedance elements over a wide frequency range of 1 kHz–10 MHz. (a) z_{11} frequency response. (b) z_{12} frequency response.

$$\mathbf{Z_1} = \begin{bmatrix} 1001.0\angle 89.6^o & 978.9\angle 89.6^o & 970.1\angle 89.6^o & 985.2\angle 89.6^o \\ 978.9\angle 89.6^o & 1011.4\angle 89.6^o & 967.0\angle 89.59^o & 982.6\angle 89.6^o \\ 970.1\angle 89.6^o & 967.0\angle 89.59^o & 992.6\angle 89.59^o & 976.8\angle 89.6^o \\ 985.2\angle 89.6^o & 982.6\angle 89.6^o & 976.8\angle 89.6^o & 1014.2\angle 89.61^o \end{bmatrix} \Omega. \tag{11}$$

Furthermore, the extracted ECM inductance matrix at 100 kHz following the method in [9] is given in (12), and extended to multiple harmonics using the approach in [2]

$$\mathbf{L_{ECM}} = \begin{bmatrix} 1534.80 & 1537.84 & 1522.61 & 1545.45 \\ 1537.84 & 1616.08 & 1552.42 & 1575.98 \\ 1522.61 & 1552.42 & 1584.27 & 1564.72 \\ 1545.45 & 1575.98 & 1564.72 & 1622.98 \end{bmatrix} \mu\text{H}. \tag{12}$$

The Y-model is extracted using a least-squares best-fit approach to mitigate inconsistent solutions arising from unavoidable measurement errors, coupled with its reduced-order nature. L_{bx} refers to the xth-port branch leakage inductance of the HFML. From the Y-model least-squares best-fit, $L_{b1} =$

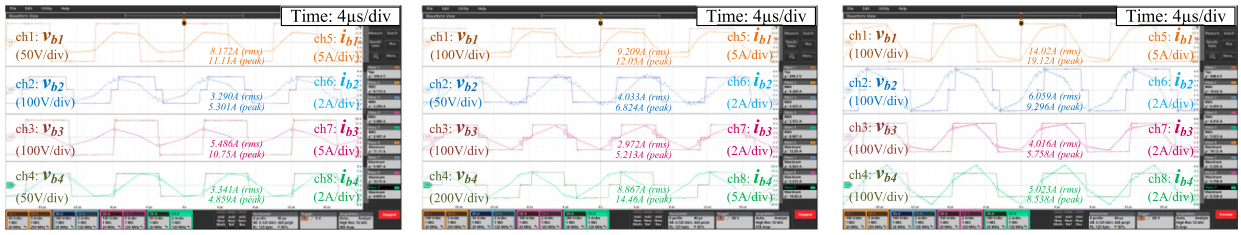

(a) (b) (c)

Fig. 6. Steady-state experimental waveforms of HFML branch voltages and currents during QAB operation where $\{[V_1, V_2, V_3, V_4], [P_1, P_2, P_3, P_4]\}$ is: (a) case 1: {[200 V, 280 V, 360 V, 120 V], [1180 W, 440 W, 500 W, 240 W]}, (b) case 2: {[300 V, 130 V, 260 V, 540 V], [2090 W, 320 W, 570 W, 1200 W]}, (c) case 3: {[400 V, 440 V, 300 V, 240 V], [3200 W, 1300 W, 900 W, 1000 W]}.

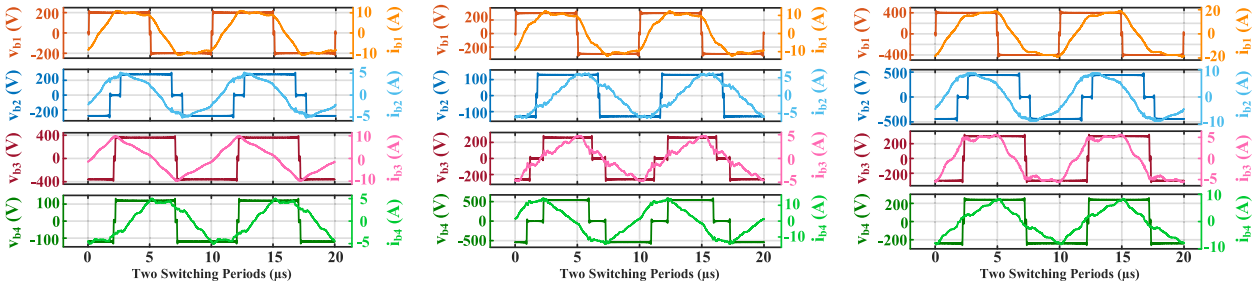

(a) (b) (c)

Fig. 7. Analytical results of the extracted **Z**-matrix HFML model using GHA while considering different steady-state operating conditions. (a) Case 1. (b) Case 2. (c) Case 3.

TABLE IV
COMPARISON OF THE EXPERIMENTALLY MEASURED, **Z**-MATRIX, ECM [9], AND Y-Δ MODEL [4] HFML BRANCH CURRENTS

Case	Method	Primary		Secondary		Tertiary		Quaternary	
		$i_{b1,\text{rms}}$ (A)	$i_{b1,\text{peak}}$ (A)	$i_{b2,\text{rms}}$ (A)	$i_{b2,\text{peak}}$ (A)	$i_{b3,\text{rms}}$ (A)	$i_{b3,\text{peak}}$ (A)	$i_{b4,\text{rms}}$ (A)	$i_{b4,\text{peak}}$ (A)
Case 1	Measured	8.172	11.11	3.29	5.301	5.486	10.75	3.341	4.859
	Z-Matrix	8.241	11.002	3.376	5.137	5.756	9.956	3.252	5.009
	ECM	9.513	12.21	3.826	5.664	6.483	11.041	3.468	4.753
	Y-Δ	8.355	10.632	3.035	4.597	5.699	9.69	3.208	4.797
Case 2	Measured	9.209	12.05	4.033	6.824	2.972	5.213	8.867	14.46
	Z-Matrix	9.073	12.421	4.04	6.307	2.752	4.791	9.095	14.502
	ECM	10.223	12.411	4.648	7.25	3.115	5.227	9.505	14.68
	Y-Δ	9.455	12.165	4.078	6.016	2.78	4.622	9.62	14.888
Case 3	Measured	14.02	19.12	6.059	9.296	4.016	5.758	5.023	8.538
	Z-Matrix	14.032	19.072	6.26	8.86	4.165	5.664	4.838	8.382
	ECM	16.126	21.904	7.254	10.406	4.796	6.609	5.066	8.458
	Y-Δ	14.253	19.498	5.794	8.512	4.344	6.049	5.331	8.814

31.815 μH, $L_{b2} = 57.198$ μH, $L_{b3} = 50.774$ μH, $L_{b4} = 35.863$ μH. Thereafter, the Y-Δ model is calculated at 100 kHz using [4], while assuming a negligibly large magnetizing branch. The result is expressed in (13) where L_{xy} is the Δ-equivalent link inductance between ports x and y

$$\mathbf{L_{Y-\Delta}} = \begin{bmatrix} L_{12} & L_{13} & L_{14} \\ L_{23} & L_{24} & L_{34} \end{bmatrix} = \begin{bmatrix} 176.759 & 156.911 & 110.828 \\ 282.094 & 199.246 & 176.870 \end{bmatrix} \mu\text{H}. \quad (13)$$

The analytical results of the extracted **Z**-matrix, ECM, and Y-Δ models in (11), (12), and (13) are benchmarked against the steady-state four-port MAB (QAB) experimental results.

C. Steady-State Performance

QAB steady-state experiments are conducted across three different operating cases, as shown in Fig. 6. The loss minimization algorithm in [12] is used to generate the corresponding optimal modulation parameters (φ_x, δ_x). Using the GHA construct in Section III, the extracted **Z**-matrix can be utilized to analytically recreate the steady-state converter operation, as demonstrated in Fig. 7. In this regard, the extracted **Z**-matrix is used to analytically estimate the rms and peak values of the HFML

branch currents, which is thencompared with the other existing HFML models.

D. Discussion

The detailed results of the experimentally measured rms and peak branch currents from the QAB steady-state cases in comparison with the extracted **Z**-matrix, ECM [9] and Y-Δ [4] models are presented in Table IV. Note that deadtime effects are excluded from the analytical models. The observable deviations in the ECM can be ascribed to its error-prone, concurrent two-port voltage-current measurements, along with the use of short-circuits with nonnegligible impedances. Whereas, the deviations with the Y-Δ model are attributed to its reduced-order nature precluding it from fully capturing the asymmetric cross-coupling relationships within the HFML. Hence, the summarized results in Table IV indicate that the **Z**-matrix analytical values yield the closest estimates to the measured values while considering the HFML port-wise current-flow dynamics. This validates the accuracy of the extracted full-order **Z**-matrix while utilizing the proposed single-port impedance measurement scheme.

VI. Conclusion

This letter presents a novel single-port impedance measurement methodology for the parameter extraction of a full-order **Z**-matrix HFML model for an n-port MAB converter. The extracted **Z**-matrix is subsequently utilized in a GHA framework. To validate the accuracy of the extracted **Z**-matrix in analytically predicting the HFML branch currents, steady-state QAB experiments are conducted across multiple cases. Thereafter, the extracted **Z**-matrix is then benchmarked against the extracted ECM, and Y-Δ (star-delta) model. The comparative analysis indicates that the extracted **Z**-matrix yields the most accurate rms and peak branch current estimates which validates the accuracy of the proposed single-port impedance measurement scheme.

Acknowledgment

The authors would like to thank Dr. Rakesh Resalayyan for his invaluable technical contributions, and ROHM Semiconductor for the SiC MOSFETs used in the MAB prototype.

References

[1] P. Koohi et al., "A dynamically reconfigurable multi-active bridge converter with extended topology-level decoupling," *IEEE Trans. Transp. Electrific.*, vol. 11, no. 5, pp. 11138–11149, Oct. 2025.

[2] Y. Chen, P. Wang, Y. Elasser, and M. Chen, "Multicell reconfigurable multi-input multi-output energy router architecture," *IEEE Trans. Power Electron.*, vol. 35, no. 12, pp. 13210–13224, Dec. 2020.

[3] Y. Park, S. Chakraborty, and A. Khaligh, "DAB converter for EV onboard chargers using bare-die SiC MOSFETs and leakage-integrated planar transformer," *IEEE Trans. Transp. Electrific.*, vol. 8, no. 1, pp. 209–224, Mar. 2022.

[4] S. Falcones, R. Ayyanar, and X. Mao, "A DC–DC multiport-converter-based solid-state transformer integrating distributed generation and storage," *IEEE Trans. Power Electron.*, vol. 28, no. 5, pp. 2192–2203, May 2013.

[5] S. Dey and A. Mallik, "Switching network loss minimization through multivariable modulation in a multiactive bridge converter," *IEEE Trans. Ind. Electron.*, vol. 70, no. 11, pp. 10833–10847, Nov. 2023.

[6] C. Gao et al., "Research on power decoupling and optimal control of modular multiactive bridge converter with relay port," *IEEE Trans. Power Electron.*, vol. 40, no. 4, pp. 5292–5308, Apr. 2025.

[7] H. Qin, H. Zhang, M. Liu, and C. Ma, "Comparison of different multiwinding transformer models in multiport AC-coupled converter application," in *Proc. 47th Annu. Conf. IEEE Ind. Electron. Soc.*, 2021, pp. 1–6.

[8] S. Dey, C. Reece, O. P. Irabor, and A. Mallik, "Comparative analysis and optimization of triple active bridge transformer configuration with integrable leakage inductance," *IEEE J. Emerg. Sel. Top. Power Electron.*, vol. 11, no. 5, pp. 5102–5119, Oct. 2023.

[9] R. Erickson and D. Maksimovic, "A multiple-winding magnetics model having directly measurable parameters," in *Proc. 29th Annu. IEEE Power Electron. Spec. Conf.*, 1998, pp. 1472–1478.

[10] A. Omidi et al., "An approach to on-trace current sensing scheme with switching noise immunity," *IEEE Sens. Lett.*, vol. 9, no. 7, Jul. 2025, Art. no. 2502904.

[11] M. Shah and K. Ngo, "Parameter extraction for the extended cantilever model of magnetic component windings," *IEEE Trans. Aerosp. Electron. Syst.*, vol. 36, no. 1, pp. 260–266, Jan. 2000.

[12] C. Singhabahu, A. Ajiboye, R. Resalayyan, A. Singh, A. Hasnain, and A. Khaligh, "Modeling and optimal modulation of MAB converter using full-order impedance matrix," *IEEE Trans. Power Electron.*, vol. 39, no. 11, pp. 15231–15241, Nov. 2024.

[13] A. Ajiboye, A. S. Gamwari, R. Resalayyan, and A. Khaligh, "Modelling the effect of the DC link decoupling capacitor of a commutation power loop using a Thevenin-based frequency domain approach," in *Proc. 2024 IEEE Appl. Power Electron. Conf. Expo.*, 2024, pp. 645–652.

[14] A. S. Gamwari, A. Ajiboye, R. Resalayyan, and A. Khaligh, "Modeling the effect of gate-drain parasitic capacitance of a SiC MOSFET in a half-bridge during the soft turn-off and hard turn-on transition," in *Proc. 2024 IEEE Appl. Power Electron. Conf. Expo.*, 2024, pp. 2419–2424.